



HAL
open science

Typology of the flow structures in dividing open channel flows

Adrien Momplot, Gislain Lipeme Kouyi, Emmanuel Mignot, Nicolas Rivière,
Jean-Luc Bertrand-Krajewski

► **To cite this version:**

Adrien Momplot, Gislain Lipeme Kouyi, Emmanuel Mignot, Nicolas Rivière, Jean-Luc Bertrand-Krajewski. Typology of the flow structures in dividing open channel flows. *Journal of Hydraulic Research*, 2017, 55 (1), pp.63-71. 10.1080/00221686.2016.1212409 . hal-01724972

HAL Id: hal-01724972

<https://hal.science/hal-01724972>

Submitted on 1 Apr 2019

HAL is a multi-disciplinary open access archive for the deposit and dissemination of scientific research documents, whether they are published or not. The documents may come from teaching and research institutions in France or abroad, or from public or private research centers.

L'archive ouverte pluridisciplinaire **HAL**, est destinée au dépôt et à la diffusion de documents scientifiques de niveau recherche, publiés ou non, émanant des établissements d'enseignement et de recherche français ou étrangers, des laboratoires publics ou privés.

35 processes. The general pattern of a steady subcritical 3-branch bifurcation is described by
36 Neary *et al.* (1999). A three-dimensional recirculating region develops in the lateral branch
37 and secondary flows appear in both outlets. Mignot *et al.* (2014) detailed the mixing layer
38 taking place at the frontier between the main flow and the recirculation zone in the lateral
39 branch. Recirculation zones, also defined as bubbles, are encountered in various geometries as
40 listed by Li and Djilali (1995).

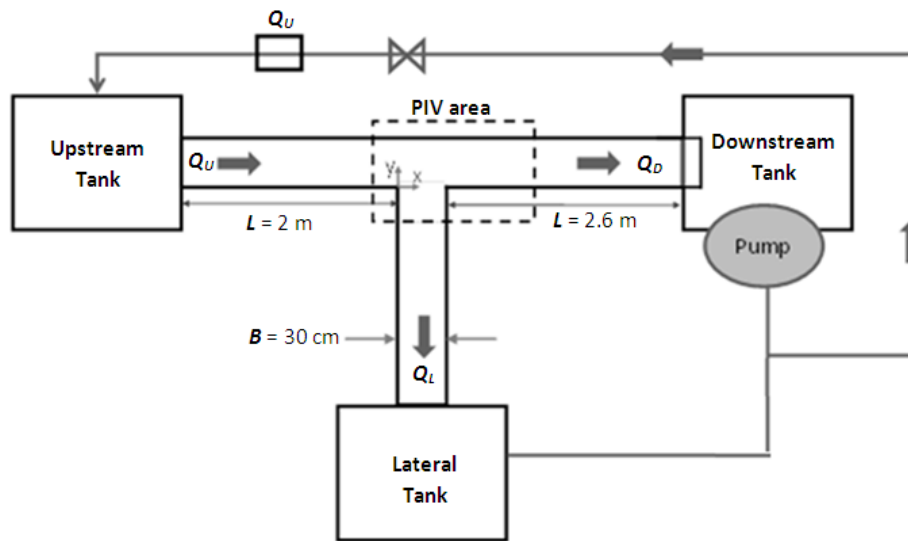
41 Regarding specifically the recirculation zone, authors such as Kasthuri and
42 Pundarikanthan (1987), Shettar and Murthy (1996) and Neary *et al.* (1999) sketch the
43 recirculation zone (in top view) as a closed semi-elliptic region developing along the
44 upstream wall of the lateral branch with maximum length and width at the free-surface and
45 minimum extensions in the near-bed region. Kasthuri and Pundarikanthan (1987) and Shettar
46 and Murthy (1996) respectively measure and compute the free-surface length and width of
47 this recirculation zone. The authors agree that as the relative lateral discharge increases, the
48 dimensions of the recirculation zone decreases. Neary *et al.* (1999) then compute flow
49 configurations with varying channel width ratios and dimensionless water depths and exhibit
50 varying characteristics of the recirculation zone pattern without clear explanation of the
51 different types of recirculation zones.

52 The aim of the present paper is twofold: first to describe the two main flow structures
53 that can be observed in the lateral branch of a 90° bifurcation and second to determine the
54 flow conditions for which each structure is observed. The paper is organized as follows: after
55 presenting the experimental and numerical approaches, the characteristics of the different
56 types of recirculation zones are described based on two measured and computed flows (F1
57 and F2) and finally a campaign of numerical simulations (including 16 different cases) is led
58 in order to establish the flow typology.

59 **2 Material and methods**

60 *2.1 Experimental set up*

61 The experimental set-up (see Fig. 1) is a horizontal 3-branch equal width ($B=30$ cm) glass
62 open-channel bifurcation of 2 and 2.6 meters long channels for the inlet and both outlet
63 respectively. Boundary conditions are the inlet discharge Q_U (measured by a flow-meter in the
64 pumping loop) and the weir crest height C_D and C_L at the downstream end of each of the two
65 outlet channels. The water depths in the upstream, lateral and downstream branches are
66 defined as h_U , h_L and h_D respectively and are measured using a digital point gauge. The
67 discharge distribution Q_L/Q_U in the bifurcation is measured through an additional flow-meter
68 in the pumping loop. In the studied cases, flow conditions are sub-critical everywhere. Details
69 about this set-up are available in Mignot *et al.* (2013 and 2014).



71
72 Figure 1. Experimental set up used for flow validation.

73 2.2 Modelling strategy

74 Numerical simulations are performed under the commercial software ANSYS Fluent version
75 14.0, following the modelling strategy proposed by Momplot *et al.* (2013) for computing
76 bifurcation flow F0 (see Table 1), these simulations are confronted with PIV measurements of
77 the horizontal velocity fields (see Fig. 2). Overall performances are fair. Additionally,
78 simulated discharge repartition and measured discharge repartition shows fair agreement
79 (differences are less than 10%).

80 Table 1. Characteristics of the validated flow.

Flow id.	Inlet discharge Q_U ($L \cdot s^{-1}$)	Weir crest height h_{crest} (m)	Discharge distribution (Q_L/Q_U)	Froude Number in upstream channel (-)	Upstream aspect ratio B/h_U (-)
F0	4	0.12	0.51	0.102	2.5

81

82 The model solves the RANS (Reynolds Averaged Navier-Stokes) equations using the
83 Volume of Fluid - VOF -method for computing the free-surface curve and a Reynolds stress
84 model - *RSM* - as turbulence model for system closure (see Launder *et al.*, 1975). *Scalable*
85 wall-functions (see Grotjans and Menter, 1998) are used for walls; a uniform velocity U_{Inlet} is
86 set at the inlet cross-section; atmospheric pressure P_0 is set at the top of the computational
87 domain and at outlets. Crest heights are explicitly represented in the mesh. After the weirs,
88 standard pressure outlet conditions are set. Discretisation scheme use for pressure is *Body-*
89 *Force Weighted* and *Second-Order Upwind* for other variables. Pressure-velocity coupling
90 algorithm is *PISO*.

91

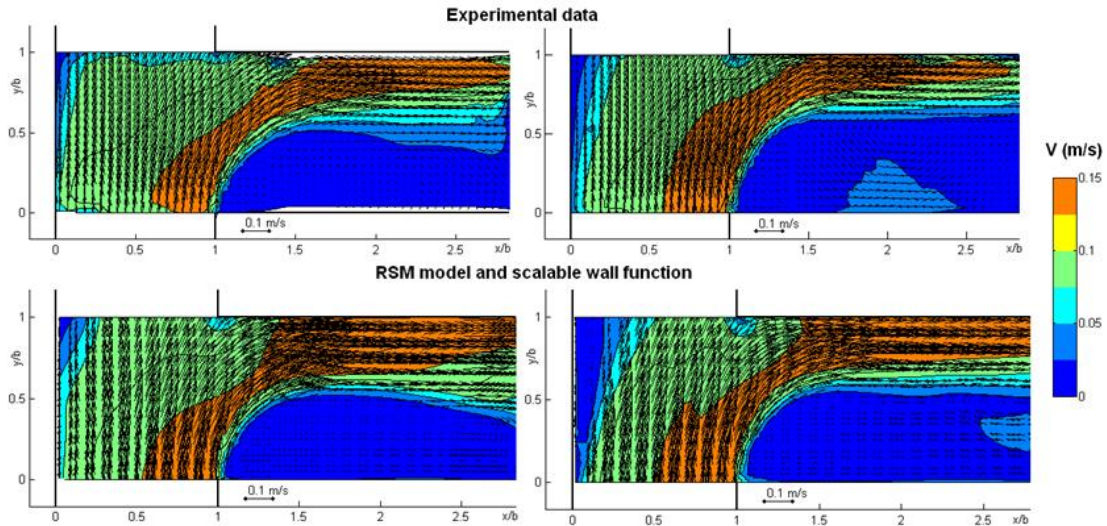
92 Mesh independency is verified using the grid convergence index (GCI) defined by
 93 Roache (1994) as:

$$94 \quad GCI_X = \frac{(X_F - X_C) \cdot r^p}{r^p - 1}$$

Equation 1

95 With :
 96 - GCI_X : the simulation error on variable X due to the fine mesh (dimension of
 97 X), X can be a discharge, a water depth, a velocity, etc.
 98 - X_F : the simulated variable X for the fine mesh (dimension of X)
 99 - X_C : the simulated variable X for the coarse mesh (dimension of X)
 100 - r : the ratio $\frac{N_F}{N_C}$, N_F being the fine mesh number of cells and N_C the coarse
 101 mesh number of cells (dimensionless)
 102 - p : the discretisation schemes order (dimensionless).

103 The GCI_X value is an estimator of the error committed on the true variable X value
 104 that is due to the mesh. Mesh independency is obtained when the relative error is below 5%.



105 Figure 2. Confrontation between PIV measurements of horizontal velocity fields (top) and
 106 simulated horizontal velocity fields (bottom) for two elevation: $z = 4$ cm (left) and $z = 9$ cm
 107 (right).
 108

109 3 Flow structure description

110 Table 2. Cases F1 and F2 studied experimentally and numerically exhibiting respectively a
 111 “helix-shaped” recirculation and a “closed” recirculation structure in the lateral branch.

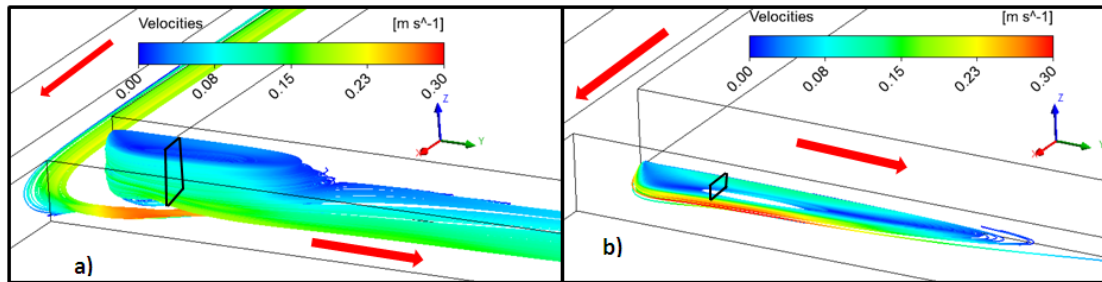
Flow id.	Inlet discharge Q_U ($L \cdot s^{-1}$)	Weir crest height h_{crest} (m)	Discharge distribution (Q_L/Q_U)	Froude Number in upstream channel (-)	Upstream aspect ratio B/h_U (-)
F1	8	0.09	0.47	0.218	2.50
F2	4	0.025	0.50	0.448	6.69

112
 113

114 Table 3. GCI analysis for flow F1 and F2.

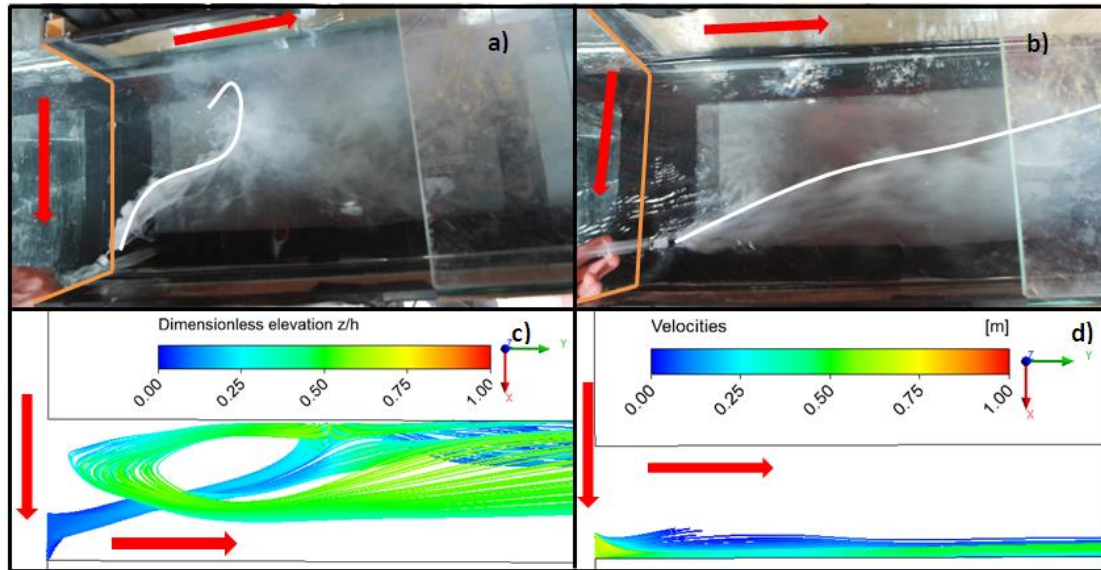
F1 - $h_{crest} = 9 \text{ cm}$ $Q_U = 8 \text{ L/s}$ -				
	Base mesh	GCI mesh	Absolute mesh error	Relative mesh error
Mesh size (cells)	738000	461500	-	-
$Q_D \text{ (m}^3\cdot\text{s}^{-1}\text{)}$	4.320	4.352	0.053	0.012
$Q_L \text{ (m}^3\cdot\text{s}^{-1}\text{)}$	3.743	3.706	0.061	0.016
$U_{moy-U} \text{ (m}\cdot\text{s}^{-1}\text{)}$	0.237	0.24	0.005	0.021
$U_{moy-L} \text{ (m}\cdot\text{s}^{-1}\text{)}$	0.1104	0.1108	0.001	0.006
F2 - $h_{crest} = 2.5 \text{ cm}$ $Q_U = 4 \text{ L/s}$ -				
	Base mesh	GCI mesh	Absolute mesh error	Relative mesh error
Mesh size (cells)	756000	412500	-	-
$Q_D \text{ (m}^3\cdot\text{s}^{-1}\text{)}$	2.276	2.343	0.110	0.048
$Q_L \text{ (m}^3\cdot\text{s}^{-1}\text{)}$	1.762	1.744	0.030	0.017
$U_{moy-U} \text{ (m}\cdot\text{s}^{-1}\text{)}$	0.388	0.379	0.015	0.038
$U_{moy-L} \text{ (m}\cdot\text{s}^{-1}\text{)}$	0.211	0.21	0.002	0.008

115



116

117 Figure 3. Two flow structures in the lateral branch of a bifurcation flow: a) a helix-shaped
 118 recirculation for flow F1 and, b) a closed recirculation for F2. Drawn streamlines are the ones
 119 going through the white plane located in the lateral branch at a distance equal to 1B from the
 120 entry section, covering the whole water depth and extending transversally from the left bank
 121 to the streamlines that separates at the corner between the upstream and lateral branches. This
 122 plane permits to enclose the whole recirculation. Red arrows indicate the main flow
 123 directions.



124
 125 Figure 4. Laboratory and simulation observations of two different flow structures in the
 126 lateral branch of two bifurcation flows: F1 (a-c) and F2 (b-d). (a-b) show experiments, (c-d)
 127 show numerical streamlines colored by the dimensionless elevation z/h_L (from blue, being the
 128 bottom of the channel; to red, being the free-surface). For (a-b), a white dye tracer is injected
 129 in the downstream corner of the lateral channel, near the bottom, the white line represents the
 130 limit of the tracer extension, red arrows indicate flow directions and orange lines mark the
 131 inlet section of the lateral branch.

132

133 Among all studied flows, two recirculation structures could be observed. Table 2 presents two
 134 flow cases investigated numerically and experimentally, each one exhibits a different
 135 recirculation structure: a so-called “helix shaped” for F1 and a “closed” one for F2. Fig. 4
 136 shows numerical results for these flow cases and particularly the behaviour of some selected
 137 streamlines. Fig. 4 compares experimental observations for the two flow cases regarding the
 138 transport of white dye tracer in the lateral branch and numerical streamlines obtained through
 139 RANS simulations. In both cases, injection takes place near the bottom part of the
 140 downstream corner region. These results confirm the fair agreement between simulated and
 141 measured flow patterns. Additionally, results of the GCI analysis displayed in Table 3
 142 indicates that meshes used to compute both flows are efficient for the prediction of discharge
 143 and bulk velocities in the lateral branch. Surprisingly, the mesh for flow F2 is less efficient
 144 for discharge and velocities representation in the upstream branch than the mesh for flow F1.

145

The two figures permit to describe both recirculation structures:

146

- The closed recirculation observed for flow F2 is a 2D semi-elliptic closed region
 147 developing along the upstream wall of the lateral branch as described in the literature: no flow
 148 enters or leaves this region and it is of larger streamwise and transverse extension at the free-
 149 surface than near the bed (Fig. 3b). Consequently, the streamlines starting from the

150 downstream corner of the intersection remain quite parallel to the banks of the lateral channel
151 towards downstream and do not interact with the recirculation zone (Fig. 4b).

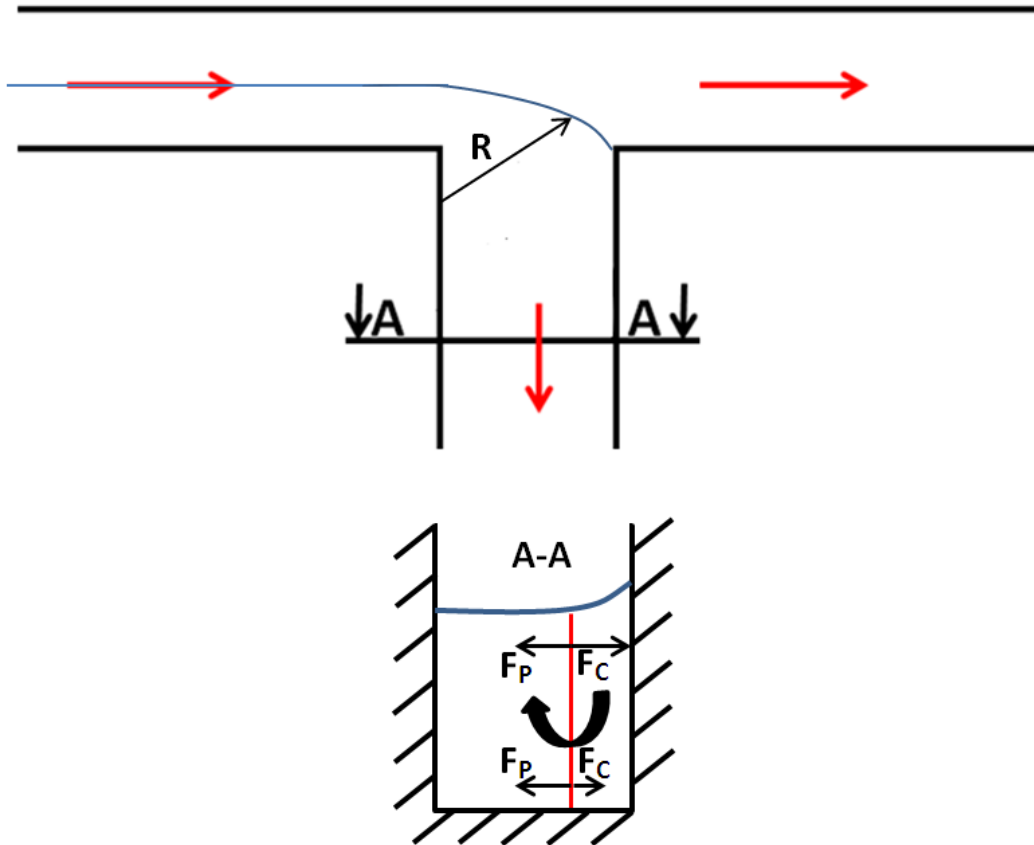
152 - The helix-shaped recirculation observed for flow F1 is a 3D ascendant flow (see Fig.
153 3a and 4c): i. supplied by the bottom flow of the upstream channel, ii. entering the lateral
154 branch near the bottom part of the downstream corner area, iii. approaching the opposite
155 (upstream) wall of the lateral branch, iv. raising towards the free-surface, first in the direction
156 of the intersection (towards upstream) and then towards downstream along center of the
157 branch. v. escaping towards downstream in the upstream half of the branch. Consequently, the
158 streamlines starting from the downstream corner of the intersection enter the recirculation
159 structure (Fig. 4a). These two distinct flow structures corroborate the different streamlines
160 plots near the bottom reported by Neary *et al.* (1999) in their figure 10 and the pathlines in
161 their figure 11c.

162 **4 Flow typology**

163 In order to establish the flow conditions for which each recirculation structure is observed, a
164 flow typology is established following the parameters obtained through dimensional analysis.
165 Using the same approach as Mignot *et al.* (2013) and assuming (as for the authors) that the
166 flow is turbulent (see Table 10) and smooth, the 8 parameters governing the flow
167 characteristics are: the three discharges (Q_U , Q_L , Q_D), the three water depths (h_U , h_L , h_D) and
168 the two weir crest heights (C_D , C_L). Mass conservation equation ($Q_U = Q_L + Q_D$) permits to
169 remove one parameter (Q_L); both known stage discharge equations ($h_D = f(Q_D, C_D)$ and $h_L =$
170 $f(Q_L, C_L)$) permit to remove h_L and C_D ; the momentum equation introduced by Ramamurthy *et*
171 *al.* (1990) permits to remove h_D ; the empirical closure equation introduced by Rivière *et al.*
172 (2007) permits to remove Q_D ; finally, the following simplification considered in the present
173 work $C_D = C_L$ permits to remove C_L . We end up with the two remaining parameters Q_U and h_U ,
174 which can be transformed (see Mignot *et al.*, 2013) as dimensionless independent parameters:
175 upstream Froude number Fr_U and upstream aspect ratio B/h_U . Note that the present
176 simplification $C_D = C_L$ is responsible for the reduction of independent parameters from 3 in
177 Mignot *et al.* (2013) to 2 in the present work and leads to a discharge distribution Q_L/Q_U of
178 about 45 to 55%.

179 The aim of the part being a flow typology assessment for a recirculation zone, a quick
180 look at others recirculation zone typologies is needed. There is many situations leading to a
181 recirculation zone (listed by Li and Djilali, 1995). For each of these situations, a flow
182 typology can be established by studying specific forces configurations. For example, Chu *et*
183 *al.* (2004) establish a typology for a recirculation zone where confinement and friction are the
184 determining forces. Dufresne *et al.* (2010) also establish a recirculation zone typology in
185 rectangular shallow reservoirs, where inertial forces and pressure/water depth gradients are

186 determining forces. These two cases lead to two different typologies. In the present case, the
 187 suspected determining forces are centrifugal force and pressure force: when the centrifugal
 188 force effect is significant, we can observe the helix-shaped recirculation because of the
 189 pressure force induce by the centrifugal force (see Fig. 5). It is similar to the tea-leaves effect.



190
 191 Figure 5. Forces balance in a lateral branch cross-section. Red arrows indicate flow
 192 directions. F_C is the volume centrifugal force (N.m^{-3}), F_P the volume pressure force (N.m^{-3}).
 193 Blue line indicates the free surface in the cross-section and R is the curvature radius of the
 194 separation.

195

196 Two forces are defined in the lateral branch cross-section A-A (see Fig. 5) as follow:

197
$$F_C = \rho \frac{U_U^2}{R}$$

198 Equation 2

199
$$F_P = \rho g$$

200 Equation 3

- 201 Where:
- 202 - F_C : the centrifugal force (N.m^{-3})
 - 203 - U_U : the mean velocity in the upstream channel (m.s^{-1})
 - 204 - R : the curvature radius of the separation (m)
 - 205 - F_P : the pressure force (N.m^{-3})
 - 206 - g : the acceleration of gravity ($= 9.81 \text{ m.s}^{-2}$)

207 A comparison between the two defined forces gives:

$$208 \quad \frac{F_C}{F_P} = \frac{\rho \frac{U_U^2}{R}}{\rho g} = \frac{U_U^2}{Rg}$$

209 Equation 4

210 It is possible to assimilate R to the channel width B . Equation 4 becomes:

$$211 \quad \frac{F_C}{F_P} = \frac{U_U^2}{Bg} = \frac{U_U^2}{\frac{B}{h_U} \cdot gh_U} = \frac{Fr_U^2}{\frac{B}{h_U}}$$

212 Equation 5

213 With: $-h_U$: the water depth in the upstream channel (m)

214 Equation 5 indicates that a relationship between the squared Froude number in the
215 upstream channel Fr_U^2 and the upstream aspect ratio B/h_U can determine the flow topology.

216 A numerical campaign is led to investigate this possible relationship.

217 Table 4 presents the numerical campaign, comprising 16 flow cases, led to establish
218 the flow typology. For each case, Froude number in upstream channel Fr_U is defined as:

$$219 \quad Fr_U = \frac{U_U}{\sqrt{g \cdot h_U}} \in [0.035; 0.558]$$

220 Reynolds number in upstream channel Re_U is defined as:

$$221 \quad Re_U = \frac{4 \cdot U_u \cdot B \cdot h_U}{\nu \cdot (B + 2 \cdot h_U)} \in [7400; 103900]$$

222 With : $-U_U$: the mean velocity in the upstream channel (m.s⁻¹)

223 $-B$: the channel width (m)

224 $-h_U$: the upstream channel water depth (m)

225 All tested cases are thus subcritical and turbulent (see Table 4).

226 For this campaign, the crest height in both outlet branches C_D and C_L ($C_D = C_L$) and
227 the upstream discharge Q_U are the two varying boundary conditions which permit to vary the
228 two independent parameters: Fr_U and B/h_U .

229

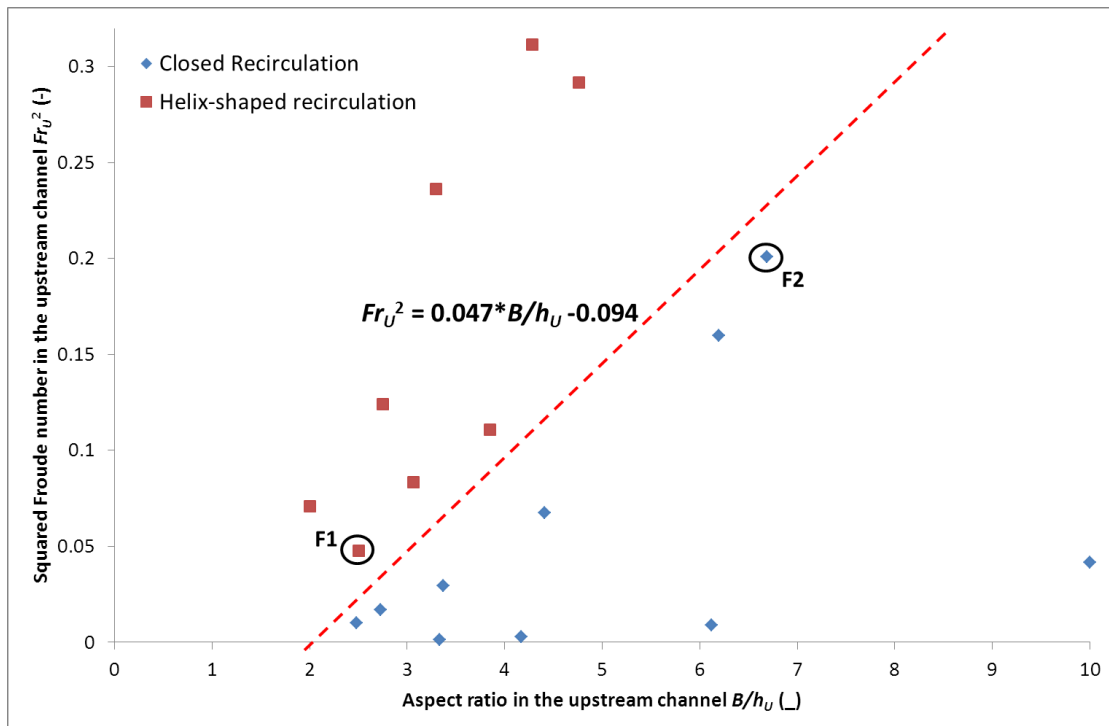
230 Table 4. Simulated cases for the typology numerical campaign.

	Crest height in downstream branches h_{crest} (m)	Inlet discharge Q_U (L.s ⁻¹)	Flow distribution (Q_L/Q_U)	Reynolds Number in upstream branch Re_U (-)	Froude Number in upstream branch Fr_U (-)	Upstream aspect ratio B/h_U (-)
Case 1	0.03	1	0.485	11066	0.204	10.00
Case 2	0.03	4	0.45	40240	0.400	6.20
Case 3	0.03	8	0.454	75340	0.540	4.76
Case 4	0.03	12	0.345	88130	0.558	4.29
Case 5	0.05	1	0.505	9700	0.095	6.12
Case 6	0.05	4	0.481	39810	0.260	4.41

Case 7	0.05	8	0.457	79070	0.333	3.84
Case 8	0.05	12	0.433	103903	0.486	3.30
Case 9	0.07	1	0.511	8504	0.052	4.16
Case 10	0.07	4	0.472	35950	0.172	3.37
Case 11	0.07	8	0.459	67260	0.289	3.06
Case 12	0.07	12	0.555	80810	0.352	2.75
Case 13	0.09	1	0.521	7400	0.035	3.33
Case 14	0.09	4	0.488	34310	0.130	2.73
Case 15	0.09	8	0.468	63070	0.218	2.50
Case 16	0.09	12	0.474	96800	0.266	2.00

231

232 Fig. 6 shows the distribution of each recirculation structure, according to two parameters:
 233 squared upstream Froude number Fr_U^2 and upstream aspect ratio B/h_U . Both regions are
 234 clearly separated from each other: a linear – at least with the present set of experiments –
 235 oblique boundary separates the two types. For low Fr_U^2 and high B/h_U values, the closed
 236 recirculation takes place whilst for high Fr_U^2 and low B/h_U values, the helix-shaped
 237 recirculation occurs.



238

239 Figure 6. Flow typology in the lateral branch. Flow F1 and F2 are circled. The red-dashed line
 240 represents the boundary between a classic recirculation in lateral branch and a helix-shaped
 241 one.

242 5 Conclusions and perspectives

243 The present papers aimed at defining the flow patterns occurring in the lateral branch of an
 244 open-channel bifurcation. A typology comprising two flow structures was established based

245 on the characteristics of the recirculation zone. The two structures are named i. “closed
246 recirculation”, similar to the flow pattern previously described in the literature and ii. “helix-
247 shaped recirculation” for which the flow pattern strongly differs and is described in the
248 present paper. Both structures were observed using both experimental and numerical
249 approaches. Following the assumptions of a smooth and turbulent flow regime and equal weir
250 crest heights at both outlets, the typology is based on the comparison between centrifugal
251 force effect and pressure force effect by the mean of squared upstream Froude number Fr_U^2
252 and upstream aspect ratio B/h_U and exhibits two clear regions of recirculation structure
253 occurrence.

254 As perspectives, bed friction effect should be investigated, as well as Reynolds number effect.
255 As the define flow topology depends on curvature radius of the separation, the effect of
256 channel width ratio and discharge repartition will have an effect and should also be
257 investigated.

258 **Acknowledgements**

259 These works are part of the laboratory of excellence IMU (Smartness on Urban Worlds) and
260 the OTHU (Field Observatory for Urban Hydrology) at Lyon. Authors would like to thank:
261 the French ministry of research for the Ph.D. funding and the ANR (National Agency for
262 research) project funding (ANR-11-ECOTECH-007-MENTOR) and the INSU (National
263 Institute for Universe Science, project EC2CO-Cytrix 2011 project No 231).

264 **Notations**

265 B = channel width (m)
266 C_L = crest height in the lateral branch (m)
267 C_D = crest height in the downstream branch (m)
268 F_C = centrifugal force ($N.m^{-3}$)
269 F_P = pressure force ($N.m^{-3}$)
270 Fr_U = Froude number in upstream channel (-)
271 GCI_X = grid convergence index value for variable X (dimension of variable X)
272 h_U = water depth in the upstream channel (m)
273 h_L = water depth in the lateral branch (m)
274 h_D = water depth in the downstream branch (m)
275 h_{crest} = crest height for case F1 and F2 (m)
276 k = wall roughness (m)
277 N_C = number of cells of the coarse mesh (-)
278 N_F = number of cells of the fine mesh (-)
279 P_0 = atmospheric pressure (Pa)
280 Q_U = upstream discharge ($L.s^{-1}$)
281 Q_L = lateral branch discharge ($L.s^{-1}$)
282 Q_D = downstream branch discharge ($L.s^{-1}$)
283 r = cell number ratio between fine mesh and coarse mesh (-)
284 R = curvature radius of the separation zone (m)
285 Re_U = Reynolds number in upstream branch (-)

286 U_{Inlet} = numerical velocity set at the inlet cross-section of the upstream channel ($\text{m}\cdot\text{s}^{-1}$)
287 U_U = mean velocity in the upstream channel ($\text{m}\cdot\text{s}^{-1}$)
288 X_C = value of variable X for coarse mesh (variable)
289 X_F = value of variable X for fine mesh (variable)
290 z = elevation (m)
291 ν = viscosity of water ($= 1\cdot 10^{-6} \text{ m}^2\cdot\text{s}^{-1}$)

292 **References**

- 293 Chu, V. H., Liu, F., & Altai, W. (2004). Friction and confinement effects on a shallow
294 recirculating flow. *Journal of Environmental Engineering and Science*, 3(5), 463-475.
- 295 Dufresne, M., Dewals, B. J., Erpicum, S., Archambeau, P., & Piroton, M. (2010).
296 Experimental investigation of flow pattern and sediment deposition in rectangular
297 shallow reservoirs. *International Journal of Sediment Research*, 25(3), 258-270.
- 298 Grace, J. L. & Priest, M. S. (1958). Division of flow in open channel junctions. *Bulletin*
299 *No.31. Engineering Experiment Station*, Alabama Polytechnic Institute.
- 300 Grotjans H. & Menter F. R. 1998. Wall functions for industrial applications. In Proceedings
301 of *Computational FluidDynamics'98, ECCOMAS*, 1(2), Papailiou KD (ed.). Wiley:
302 Chichester, U.K.. 1112–1117
- 303 Hsu, C. C., Tang, C. J., Lee, W. J. & Shieh, M. Y. (2002). Subcritical 90 equal-width open-
304 channel dividing flow. *Journal of Hydraulic Engineering*, 128(7), 716-720.
- 305 Kasthuri B. & Pundarikanthan N. V. (1987). Discussion of “Separation zone at open channel
306 junctions”. *Journal of Hydraulic Engineering*, 113(4), 543.
- 307 Launder B. E., Reece G. J. & Rodi W. (1975). Progress in the Development of a Reynolds-
308 Stress Turbulence Closure. *Journal of Fluid Mechanics*. 68(3). 537–566
- 309 Li X. & Djilali N. (1995). On the scaling of separation bubbles. *JSME international journal*.
310 *Series B, fluids and thermal engineering*, 38(4), 541-548. Mignot, E., Zeng, C.,
311 Dominguez, G., Li, C. W., Rivière, N. & Bazin, P. H. (2013). Impact of topographic
312 obstacles on the discharge distribution in open-channel bifurcations. *Journal of*
313 *Hydrology*, 494, 10-19.
- 314 Mignot, E., Doppler, D., Riviere, N., Vinkovic, I., Gence, J. N. & Simoens, S. (2014).
315 Analysis of flow separation using a local frame-axis: application to the open-channel
316 bifurcation. *Journal of Hydraulic Engineering*. 280-290.
- 317 Momplot, A., Lipeme Kouyi, G., Mignot, E., Rivière, N. & Bertrand-Krajewski, J.-L. (2013)
318 URANS Approach for Open Channel Bifurcation Flows Modelling. *7th International*
319 *Conference on Sewer Processes and Network*, Sheffield, August 2013, 8 pages.
- 320 Neary, V. S., Sotiropoulos, F. & Odgaard A. J. (1999). Three-dimensional numerical model
321 of lateral intake inflows. *Journal of Hydraulic Engineering*, 125(2), 126-140.

- 322 Ramamurthy, A. S., Tran, D. M. & Carballada, L. B. (1990). Dividing flow in open channels.
323 *Journal of Hydraulic Engineering*, 116(3), 449-455.
- 324 Ramamurthy, A. S., Qu, J. & Vo, D. (2007). Numerical and experimental study of dividing
325 open-channel flows. *Journal of Hydraulic Engineering*, 133(10), 1135-1144.
- 326 Rivière, N., Travin, G. & Perkins R. J. (2007). Transcritical flows in open channels junctions.
327 *Proceedings, 32nd IAHR Congress, Venice, Italy, IAHR, paper SS05-11.*
- 328 Rivière, N., G. Travin, and R. J. Perkins (2011), Subcritical open channel flows in four branch
329 intersections, *Water Resour. Res.*, 47, W10517, doi:10.1029/2011WR010504.
- 330 Shettar, A. S. & Keshava Murthy, K. (1996). A numerical study of division of flow in open
331 channels. *Journal of Hydraulic Research*, 34(5), 651-675.